JACS
JOURNAL OF THE AMERICAN CHEMICAL SOCIETY

Article

pubs.acs.org/JACS

Applications of NMR Crystallography to Problems in Biomineralization: Refinement of the Crystal Structure and ^{31}P Solid-State NMR Spectral Assignment of Octacalcium Phosphate

Erika Davies,[†] Melinda J. Duer,*[,†] Sharon E. Ashbrook,[‡] and John M. Griffin[‡]

[†]Department of Chemistry, Lensfield Road, University of Cambridge, Cambridge CB2 1EW, U.K.

[‡]School of Chemistry and EaStCHEM, North Haugh, University of St Andrews, St Andrews KY16 9ST, U.K.

Supporting Information

ABSTRACT: By combining X-ray crystallography, first-principles density functional theory calculations, and solid-state nuclear magnetic resonance spectroscopy, we have refined the crystal structure of octacalcium phosphate (OCP), reassigned its ^{31}P NMR spectrum, and identified an extended hydrogen-bonding network that we propose is critical to the structural stability of OCP. Analogous water networks may be related to the critical role of the hydration state in determining the mechanical properties of bone, as OCP has long been proposed as a precursor phase in bone mineral formation. The approach that we have taken in this paper is broadly applicable to the characterization of crystalline materials in general, but particularly to those incorporating hydrogen that cannot be fully characterized using diffraction techniques.

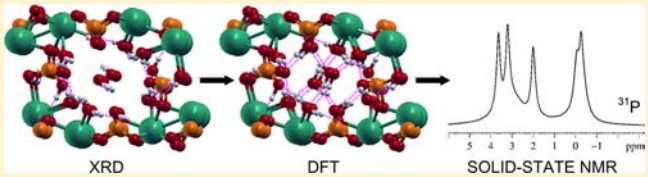

INTRODUCTION

There is growing interest in the area of "NMR crystallography", the name given to the combined application of solid-state nuclear magnetic resonance spectroscopy (NMR), X-ray diffraction (XRD) techniques, and/or first-principles calculations, to obtain structural information that would prove difficult (or impossible) to determine using any one of these techniques in isolation.[1,2] A compelling illustration of the utility of this approach is the recent identification of the main tautomeric form of 8-hydroxycarbostyril, with obvious applications in medical chemistry.[3] A combined density functional theory (DFT) and solid-state NMR investigation of the calcium phosphate phases implicated in biomineralization processes has shown an impressive correspondence between the predictions of DFT calculations and the experimental data.[4] Furthermore, first-principles calculations have recently been used to correct a tentative spectral assignment of the various ^{17}O environments found in the enstatite polymorphs of $MgSiO_3$.[5] This latter example sets an important precedent for the establishment of unequivocal spectral assignments for crystalline systems, based on a combination of experimental evidence from solid-state NMR spectroscopy and DFT calculations performed on geometry-optimized structures.

Effective treatment of bone-related conditions such as osteoporosis, osteoarthritis, and, more fundamentally, fracture due to trauma is increasingly important as the global population ages. The efficacy of drug-mediated treatments is dependent on our understanding of the nature of bone and the interfaces that exist between its organic and inorganic components. This in turn relies upon a complete description of the structure of the inorganic phase, which we shall refer to as biological apatite. An interesting calcium phosphate phase that possesses a layered structure and has been proposed as a precursor phase in the formation of biological apatite is octacalcium phosphate (OCP, $Ca_8(HPO_4)_2(PO_4)_4{\cdot}5H_2O$), shown in Figure 1.[6−8]

Early references to OCP describe its crystallography as "obscure" and dispute its very existence as a discrete calcium phosphate phase.[9] These doubts were silenced when the crystal structure of OCP was published in 1957; however, the structure was not refined to include the (likely) positions of the hydrogen atoms until 1988.[10] The first complete assignment of the ^{31}P solid-state NMR spectrum of OCP was made in 2004, based on a combination of ^{31}P double-quantum (DQ) and ^{31}P{^{1}H} heteronuclear correlation (HETCOR) spectroscopy.[11]

The *hydrated layer* in OCP, corresponding to the central region in Figure 1, is of particular interest as a model of the hydrated surface of the mineral nanocrystals in bone. This idea was first proposed by Walter E. Brown, who observed that the (100) planes of hydroxyapatite could dominate the surface area of apatite crystals [recent work has shown that (100) is a major contributor to the surface area of hydroxyapatite nanocrystals[12]], and that the layering in OCP was also parallel to the (100) face.[13] He concluded that "the structure of the water layer may prove to be a useful model for describing the interface between the apatite crystal and the aqueous phase." When dealing with crystalline materials at the nanoscale, such as biological apatite, it is the surface structure rather than the bulk properties that govern the behavior of the material. Modeling surface behavior using DFT typically requires

Received: February 22, 2012
Published: June 29, 2012

   dx.doi.org/10.1021/ja3017544 | J. Am. Chem. Soc. 2012, 134, 12508−12515

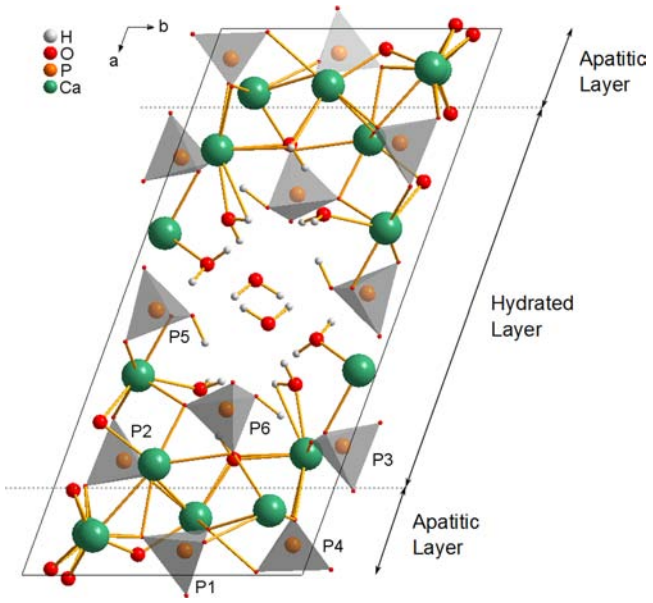

Figure 1. Unit cell of octacalcium phosphate (OCP), with regions commonly described as the *hydrated layer* and *apatitic layer* indicated. The hydrated layer contains both of the hydrogen phosphate groups (P5, P6) and two of the orthophosphate groups (P2, P3), while the remaining orthophosphate groups (P1, P4) are found within the apatitic layer. This structure has been geometry-optimized using DFT.

construction of a supercell comprising a slab terminated above and below by sufficient vacuum to preclude interaction between neighboring slabs.[14] By considering the (internal) hydrated regions of OCP as a model of the hydrated surface of biological apatite, there is no need for such measures.

While the refinement of the crystal structure of OCP published in 1988 is undoubtedly an improvement on the original structure, it nevertheless incorporates numerous unrealistic OH bond lengths (~0.8 Å, compared with a more typical value of 1.0 Å) and has large thermal parameters associated with some of the oxygen atoms. We therefore used DFT, as implemented in the CASTEP code, to determine the forces on the atoms in the structure. We found that around half of the oxygen and phosphorus atoms were subject to forces well in excess of 1 eV/Å, and that the hydrogen atoms were subject to forces as high as 17 eV/Å! Not surprisingly, then, we also found that the predicted ^{31}P isotropic chemical shifts were inconsistent with those observed experimentally (see Supporting Information).

Accordingly, in this work DFT calculations were performed to optimize the geometry of the OCP structure. In order to assess the validity of the optimized structure, the NMR parameters of the ^{31}P nuclei were then calculated and compared with experiment. This has resulted in a new assignment of the ^{31}P NMR spectrum, which resolves a key issue highlighted in the original publication and clarifies our understanding of this rather curious material. In particular, our new structure suggests that a strong, coherent hydrogen-bonding network is critical to the stability of the structure.

EXPERIMENTAL SECTION

Preparation. All reagents were purchased from Sigma-Aldrich and used without further purification. Brushite (DCPD, $CaHPO_4{\cdot}2H_2O$) was prepared by mixing aqueous solutions of $CaCl_2{\cdot}6H_2O$, Na_2HPO_4, and KH_2PO_4 at 25 °C and pH 4.2.[15] Octacalcium phosphate was prepared by the hydrolysis of brushite at 85 °C for 30 min at pH 5.[16] Brushite was obtained as a pure phase; however, the OCP showed clear evidence of apatite contamination.

All products were characterized by attenuated total reflectance Fourier transform infrared spectroscopy (FTIR-ATR), powder X-ray diffraction (PXRD), and solid-state NMR spectroscopy (see below). FTIR-ATR spectra were acquired using a PerkinElmer Spectrum One FTIR spectrometer with Universal ATR sampling accessory over the range 650−4000 cm^{-1} (resolution 4 cm^{-1}). PXRD measurements were performed on a Philips X'Pert Pro powder diffractometer equipped with an X'celerator RTMS detector and using Ni-filtered Cu K_α radiation. Samples were mounted on flat glass plates, and data collection was performed over the range 2θ = 3−80°.

NMR Measurements. All NMR measurements were performed on a Bruker 400 MHz Avance spectrometer equipped with a standard double-resonance probe at frequencies of 400.42 (^{1}H) and 162.1 MHz (^{31}P). Samples were packed into 4 mm zirconia rotors and rotated at a magic angle spinning (MAS) rate of 12.5 kHz unless otherwise stated. All samples were characterized using standard Bloch decay (BD) and cross-polarization (CP) MAS techniques (^{1}H $\pi/2$ pulse length 2.50 μs, ^{31}P $\pi/2$ pulse length 2.05 μs, ^{1}H CP field strength 82 kHz, ^{31}P CP field strength 73 kHz, ^{1}H−^{31}P CP contact time 2 ms, 6 s recycle time for CP and 1200 s recycle time for BD, broadband TPPM decoupling during signal acquisition at ^{1}H field strength 87 kHz). To investigate the changes in the ^{31}P CP spectrum of OCP with decoupling, the broadband TPPM decoupling power was also varied from 29 to 103 kHz. The ^{1}H−^{31}P HETCOR experiment was performed with frequency-switched Lee−Goldburg (FSLG) decoupling during t_1 (^{1}H field strength 100 kHz) and broadband TPPM decoupling during signal acquisition (^{1}H field strength 87 kHz). The 2D SQ−DQ ^{31}P correlation experiment was performed using the POST-C7 sequence (^{31}P field strength 88 kHz, 28 composite C7 cycles for DQ excitation and reconversion, 6 s recycle time, and broadband TPPM decoupling during signal acquisition with ^{1}H field strength 73 kHz).[17] The 2D CSA experiment was performed using the sequence developed by Orr and Duer (^{31}P field strength 83 kHz, 24 kHz sweep width in f1, MAS rate 10 kHz, and SPINAL64 decoupling during signal acquisition with ^{1}H field strength 100 kHz).[18] The ^{1}H−^{31}P−^{1}H double-CP experiments were performed using a standard double-CP sequence, modified to incorporate a *z*-filter on ^{31}P, during which time a saturation train was applied to the ^{1}H spins (^{1}H $\pi/2$ pulse length 2.50 μs, ^{31}P $\pi/2$ pulse length 2.52 μs, ^{1}H−^{31}P and ^{31}P−^{1}H CP contact times 1 ms, MAS rate 8 kHz, and 6 s recycle time).

DFT Calculations. Geometry optimizations and NMR calculations were performed using CASTEP 5.502, applying the DFT semi-empirical dispersion interaction correction (DFT-SEDC) module (G06 scheme).[19−23] The OCP structure was described as an infinite periodic solid using periodic boundary conditions and in optimizing the geometry both the lattice parameters and atomic positions were allowed to vary. The Perdew−Burke−Ernzerhof generalized gradient approximation was applied, core−valence interactions were described by ultrasoft pseudopotentials, and the wave functions were expanded using a plane-wave basis set with a kinetic energy cutoff of 680.28 eV.[24] Integrals over the Brillouin zone were performed using a 2×3×4 Monkhorst−Pack grid and no symmetry constraints were applied. [While the system has been classified as $P\bar{1}$ by single-crystal XRD, it was observed that it may in fact be $P1$.[9,10] Forcing symmetry operations in the presence of inconsistent atomic positions during DFT calculations can lead to seriously inaccurate results, hence the decision to treat the structure as $P1$.] Chemical shifts were calculated from chemical shieldings according to $\delta_{iso} \approx \sigma_{ref} - \sigma_{iso}$, where σ_{ref} = 274.4 ppm. This work was performed using the Darwin Supercomputer of the University of Cambridge High Performance Computing Service (http://www.hpc.cam.ac.uk/), provided by Dell Inc. using Strategic Research Infrastructure Funding from the Higher Education Funding Council for England. In spite of the problems associated with the use of PBE-DFT to calculate the NMR shifts of sites in close proximity to Ca atoms, development of a custom pseudopotential was beyond the scope of this work.[25]

RESULTS AND DISCUSSION

Rather than presenting the DFT calculations and experimental data separately, in the spirit of the combined approach that NMR crystallography promotes they will be introduced in this section as required to facilitate the discussion.

The first step taken in reassessing the ^{31}P NMR spectrum of OCP was to refine the crystallographic structure using CASTEP. This was particularly important since it was not possible to determine unequivocally the positions of the hydrogen atoms within the unit cell in the original X-ray crystallographic refinement, and some of the OH bond lengths in the unoptimized structure are suspiciously short (see Table 1 in the Supporting Information).[10] Hydrogen-bonding interactions are likely to be critical in stabilizing the structure of OCP, and the definitions of strong, moderate, and weak hydrogen bonds, as applied in this work, are given in Table 1.

Table 1. Defining Characteristics of Strong, Moderate, and Weak Hydrogen Bonds[26]

	strong	moderate	weak
A–H···B interaction	mostly covalent	mostly electrostatic	electrostatic
bond lengths (Å)	A–H ≈ H···B	A–H < H···B	A–H ≪ H···B
H···B	~1.2–1.5	~1.5–2.2	2.2–3.2
A···B	2.2–2.5	2.5–3.2	3.2–4.0
bond angles (°)	175–180	130–180	90–150
bond energy (kcal mol^{-1})	14–40	4–15	<4

Long-range van der Waals interactions may also play an important role in determining the structure of OCP. DFT calculations are known to struggle to accurately account for these interactions and, when gradient-corrected exchange-correlation functionals are employed, significantly overestimate the cell parameters.[27] The calculations therefore required variation in the ionic forces between consecutive iterations to be less than 0.005 eV/Å (more stringent convergence conditions are required to account for hydrogen-bonding interactions) and used the SEDC module in CASTEP to attempt to account for the long-range interactions between water molecules and HPO_4 sites.[22] The results of the geometry optimization are summarized in Table 2; for more details, as well as the results obtained in the absence of the SEDC module, refer to the Supporting Information.

Table 2. Lattice Parameters for OCP Unit Cell before and after Geometry Optimization

	before (Å)	after (Å)		before (°)	after (°)
a	19.692	19.809	α	90.15	90.35
b	9.523	9.518	β	92.54	93.30
c	6.835	6.863	γ	108.65	109.99

Broadly speaking, the optimization reinforces existing hydrogen bonds within the structure (the minimum angle associated with moderate hydrogen bonds increases from 139° to 149°) and corrects the improbably short OH bond lengths mentioned previously. More specifically, however, there are three major modifications to the structure that occur during the optimization process: a moderate (borderline strong) hydrogen bond is *formed* between P5 and P6, a moderate hydrogen bond is *reinforced* between a Ca-coordinated water molecule and P6, and three hydrogen bonds to the central water molecules are *reinforced*. A table detailing these changes can be found in the Supporting Information. It is clear that the local environments of both P5 and P6 are directly and significantly altered by these changes; however, it is important to note that the changes to the hydrogen-bonding interactions indirectly affect all of the phosphorus sites via the coordination spheres of the calcium atoms. Critically, the structural changes result in the formation of an extended hydrogen-bonding network within the hydrated layer, both in the (001) plane and parallel to the *c*-axis. A comparison between the hydrogen-bonding interactions present in the original and optimized structures is presented in Figure 2, and particular attention is drawn to the continuum formed by the hydrogen bonds between P5/P6 and P6/P3.

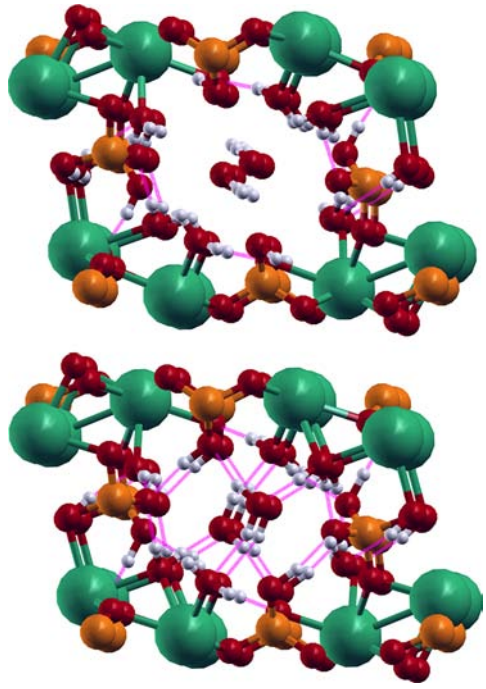

Figure 2. Hydrogen-bonding interactions (indicated by pink connecting lines) within the hydrated layers of the original (top) and relaxed (bottom) structures (note that these segments have been rotated by 90° clockwise relative to Figure 1). Images were created using XCrySDen (code available from http://www.xcrysden.org/).[28]

It is worth noting that the optimized structure is *approximately* consistent with $P\bar{1}$ symmetry (the maximum deviation from symmetry was determined by CASTEP to be 2.684×10^{-5} Å); however, given the slight inconsistencies between the atomic positions and the symmetry operations of $P\bar{1}$, it is taken to be a *P*1 system, and the unique labeling of the atoms in the supplied crystal structure has been preserved.

In order to assess how closely the geometry-optimized structure of OCP represents the "true" crystal structure of OCP, CASTEP was used to calculate the NMR shielding tensors. From these shielding tensors, it is straightforward to determine the isotropic chemical shifts for each ^{31}P environment, and these can then be compared with experimental BD and CP ^{31}P NMR spectra. Implicit in this approach is the fact that the calculated chemical shifts are those that would be observed at 0 K, and variable-temperature experimental ^{31}P NMR spectra demonstrate a linear variation in the observed ^{31}P

dx.doi.org/10.1021/ja3017544 | J. Am. Chem. Soc. 2012, 134, 12508–12515

chemical shifts with temperature (see Supporting Information). Using the gradients obtained from the linear fits to the variable-temperature data, the calculated shifts can be extrapolated to 298 K.[29] [While the range of observed chemical shifts in OCP is of the same order as the errors typically observed in DFT-based investigations of the chemical shielding parameters of ^{31}P sites in inorganic materials,[30,31] CASTEP is known to accurately predict the sign of the chemical shift differences between even slightly inequivalent sites.[32] As no crossovers were observed between the lines of best fit to the VT data, CASTEP should therefore, at worst, accurately predict the relative ordering of the sites within OCP.] A direct comparison can be then made between the calculated chemical shifts and those observed at room temperature, as per the ^{31}P BD and CP spectra presented in Figure 3.

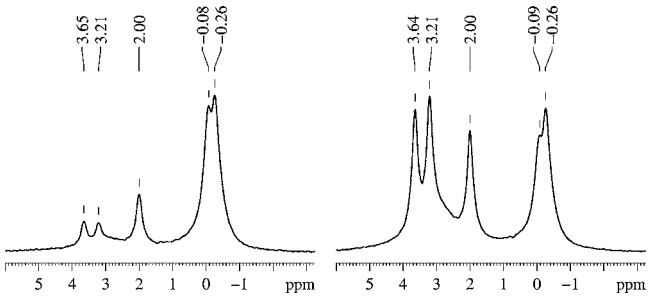

Figure 3. ^{31}P CP (left, 2 ms contact time) and ^{31}P BD (right, 1200 s recycle delay) of OCP. Note that the degree of resolution of the low-frequency signal at ∼−0.3 ppm is strongly dependent on the ^{1}H decoupling power and the MAS rate (86.5 kHz and 12.5 kHz, respectively, in this figure).

The results of this process are summarized in Table 3, together with the original spectral assignment and the assignment proposed here.[11] That this revised assignment is indeed plausible is established in the discussion that follows, with reference to the original assignment and additional experimental data.

It was noted in the previous work assigning the ^{31}P NMR spectrum of OCP that the signals in the ^{31}P BD NMR spectrum of OCP occur with an intensity ratio approximately equal to 1:1:1:3 (from high to low frequency; the signal at lowest frequency in the original work did not show any resolution) and that this conflicted with their assignment, which would be expected to give an intensity ratio of 1:2:1:2. Deconvolution of the ^{31}P BD spectrum presented in Figure 3 also gives an intensity ratio of 1:1:1:3 [treating the partially resolved lowest frequency signals at ∼0 ppm (broad peak centered at 0.08 ppm) and ∼−0.3 ppm (broad peak centered at −0.26 ppm) as one signal, as in the original work; see Supporting Information], which is entirely consistent with our revised assignment of the spectrum, guided by the chemical shift predictions of CASTEP. When the signals at ∼0 and ∼−0.3 ppm are treated separately, the signal intensity ratios are (from highest to lowest frequency again) 1:1:1:(1:2); the significance of this will become apparent in the discussion that follows.

In the previous work, the ^{31}P signal at 2 ppm was assigned to P3 based on the absence of an autocorrelation signal in the 2D POST-C7 single-quantum−double-quantum (SQ−DQ) correlation spectrum, i.e., the absence of a signal at (2 ppm, 4 ppm), see Figure 4.

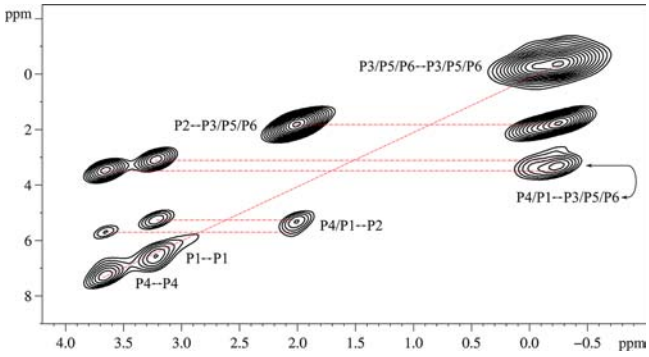

Figure 4. ^{31}P POST-C7 SQ−DQ correlation experiment indicating proximities of phosphorus sites. The distortion of the contour at approximately 3.0 ppm is due to hydroxyapatite contamination.

However, based on the P···P distances within the CASTEP-optimized structure presented in Table 4, neither P2 nor P3 is expected to yield an autocorrelation signal ($d_{P2\cdots P2} = d_{P3\cdots P3}$ = 6.86 Å). The POST-C7 data are therefore incapable of distinguishing between P2 and P3. Furthermore, they cannot be used to distinguish between P1 and P4, as both are expected to show auto-correlation peaks and to show similar patterns of cross-correlations with other ^{31}P sites. We therefore need to find other data to corroborate our revised assignment.

Close examination of the local environments of P2 and P3 reveals an initial justification of our assignment. P3, P5, and P6 are arranged so that the OH of P5 is hydrogen-bonded to P6 and the OH of P6 is hydrogen-bonded to P3, see Table 5. P3 would therefore be expected to behave more like an HPO_4 group than P2 and hence appear at lower frequency, as predicted by the CASTEP calculation.

The ^{31}P chemical shift tensor components derived from the CASTEP calculation can then be compared to experimental values determined from 2D NMR spectra, in which chemical shift anisotropy lineshapes are resolved according to their isotropic chemical shift, and the results of this are presented in Table 6.[18]

Table 3. Calculated vs Experimental ^{31}P Chemical Shifts for OCP

site[a]	calcd $\delta_{iso}^{0\ K}$ (ppm)	calcd[b] $\delta_{iso}^{298\ K}$ (ppm)	exptl $\delta_{iso}^{295\ K}$ (ppm)	original assignment[11]	new assignment
P1	1.5	3.0	3.6	P1	P4
P2	0.5	1.9	3.2	P2, P4	P1
P3	−3.4	−1.9	2.0	P3	P2
P4	2.2	3.8	−0.1	P5, P6	P6
P5	−1.6	−0.1	−0.3	P5, P6	P3, P5
P6	−0.8	0.7			

[a]As specified by CASTEP and given in the cell file. [b]Extrapolated as $\delta_{iso}^{298\ K} = 298m + \delta_{iso}^{0\ K}$; see Supporting Information for further details.

dx.doi.org/10.1021/ja3017544 | J. Am. Chem. Soc. 2012, 134, 12508−12515

Table 4. Geometry-Optimized (Minimum) Internuclear Distances Required for the Interpretation of Figure 4; Corresponding Distances Used in the Original Analysis Are Also Presented

site(s)	opt. (Å)	unopt.[11] (Å)
	Auto-Correlations	
P1	4.108	4.043
P2	6.863	6.835
P3	6.863	6.835
P4	4.056	4.041
P5	3.927	4.042
P6	6.863	6.835
	Cross-Correlations	
P2–P3	4.028	4.017
P5–P6	4.113	4.350
P3–P6	4.165	4.206
P1–P4	4.698	4.697
P2–P4	4.727	4.722
P1–P2	4.743	4.707
P2–P6	4.983	4.951
P1–P4	5.002	—
P1–P6	5.011	4.969
P1–P2	5.037	—

Table 5. Characteristics of the Hydrogen Bonding between P3, P5, and P6 (as per Table 1)

sites	$d_{O\cdots O}$ (Å)	∠O–H···O (°)	H-bond strength
P5 → P6	2.64	170	moderate
P6 → P3	2.47	176	strong

There is excellent correspondence between calculated and experimental chemical shift anisotropies for the apatitic environments P1 and P4, although their similarity again precludes verification of the relative chemical shift ordering. Good agreement is also found between calculation and experiment for P2, confirming its assignment.

Analysis of the chemical shift anisotropies and assignment of the partially resolved lowest frequency signals at ∼0 and ∼−0.3 ppm is more difficult, as from their relative intensities (as well as our revised assignment) there are contributions to the chemical shift anisotropy lineshapes from *three* ^{31}P sites in this region, viz. P3, P5, and P6. Moreover, the broadness of both these low-frequency signals and the dependence of their resolution on the ^{1}H decoupling power and MAS rate (see Figure 3) are likely to be due to molecular motion, further evidence of which can be seen in the variable-temperature ^{1}H spectra presented in Figure 5. The ^{1}H spectrum of OCP, which is dominated by the water molecules within the structure, broadens considerably between room temperature and 258 K. A more detailed picture is presented by the ^{1}H–^{31}P–^{1}H double-CP spectrum; at room temperature there is a sharp signal at 4.9 ppm, consistent with mobile water species, that is ostensibly absent in the spectrum recorded at 258 K. At 258 K, all of the water molecules are associated with the broad signal centered at 8.0 ppm, an unusually high chemical shift for water which is consistent with the water molecules being immobilized within the hydrogen-bonding network shown in Figure 2. The intensity of this broad signal is significantly enhanced at 258 K (as is the HPO_4 signal centered at 12.6 ppm), which indicates that slower molecular motions at this lower temperature are boosting the CP efficiency. Consideration of the strong hydrogen-bonding arrangement between P3, P5, and P6 (Figures 1 and 2) suggests that the motion, which clearly involves ^{1}H atoms, is likely to be ^{1}H- and/or water-hopping within this network. Any such motion means that we cannot expect exact correspondence between calculated and experimental ^{31}P chemical shifts in this region of the ^{31}P spectrum, or indeed between calculated and experimental ^{31}P chemical shift anisotropies.

Table 6. Calculated and Experimental ^{31}P Chemical Shift Anisotropy Parameters for the Phosphorus Sites in OCP, Given as the Anisotropic Principal Components of the Chemical Shift Tensor (δ_{ii}) Associated with Each Isotropic Chemical Shift (δ_{iso})

δ_{iso}^{calc} (ppm)	δ_{ii}^{calc} (ppm)[a]		site	δ_{iso}^{exp} (ppm)	δ_{ii}^{exp} (ppm)	
3.8	δ_{11}	8.2	P4	3.6	δ_{11}	9.3 ± 0.6
	δ_{22}	−1.8			δ_{22}	−0.6 ± 0.6
	δ_{33}	−6.4			δ_{33}	−9.1 ± 0.6
3.0	δ_{11}	8.7	P1	3.2	δ_{11}	11.5 ± 0.7
	δ_{22}	1.4			δ_{22}	−2.4 ± 0.5
	δ_{33}	−10.1			δ_{33}	−9.4 ± 0.6
1.9	δ_{11}	29.0	P2	2.0	δ_{11}	22.2 ± 1.3
	δ_{22}	9.8			δ_{22}	6.1 ± 1.8
	δ_{33}	−38.8			δ_{33}	−31.0 ± 2.8
0.7	δ_{11}	36.5	P6	0.0[b]	δ_{11}	20.6 ± 7.3
	δ_{22}	4.5			δ_{22}	−3.1 ± 1.5
	δ_{33}	−41.1			δ_{33}	−11.7 ± 2.2
					δ_{11}	40.1 ± 4.3
−0.1	δ_{11}	63.2	P5		δ_{22}	−13.2 ± 1.5
	δ_{22}	−21.1			δ_{33}	−40.6 ± 3.8
	δ_{33}	−42.1				
				−0.3[b]	δ_{11}	21.0 ± 2.4
−1.9	δ_{11}	25.5	P3		δ_{22}	−3.1 ± 1.5
	δ_{22}	−2.0			δ_{33}	−15.1 ± 1.8
	δ_{33}	−23.5			δ_{11}	45.2 ± 4.8
					δ_{22}	−14.9 ± 3.6
					δ_{33}	−39.2 ± 3.6

[a]Given the linear variation of the isotropic chemical shifts with temperature, the anisotropic principal components of the chemical shift tensor are not expected to exhibit any significant temperature dependence. [b]Note that the experimental measurement indicates that the sites which appear at ∼0 and ∼−0.3 ppm both have two (overlapped) chemical shift anisotropy powder patterns associated with them (see Supporting Information).

It is still possible, however, to assign the ∼0 and ∼−0.3 ppm signals and to verify that this assignment is at least consistent with the calculated chemical shifts of our revised assignment. To this end, we observed that P6 has significantly more ^{1}H atoms in close proximity than P3 or P5 (see Figure 1) and therefore investigated the comparative CP efficiencies of the partially resolved signals at low frequency. As can be seen in Figure 6, the peak at ∼0 ppm is far more intense at short CP times, and at longer CP times the peak at ∼−0.3 ppm becomes dominant.

This is consistent with the signal at ∼0 ppm being due to P6, with its greater number of neighboring ^{1}H atoms. By default, therefore, the signal at ∼−0.3 ppm is assigned to P3 and P5. That this signal arises from two overlapping peaks is consistent with the deconvolution of the ^{31}P BD spectrum discussed earlier, in which the relative intensity of this signal was found to

dx.doi.org/10.1021/ja3017544 | J. Am. Chem. Soc. 2012, 134, 12508−12515

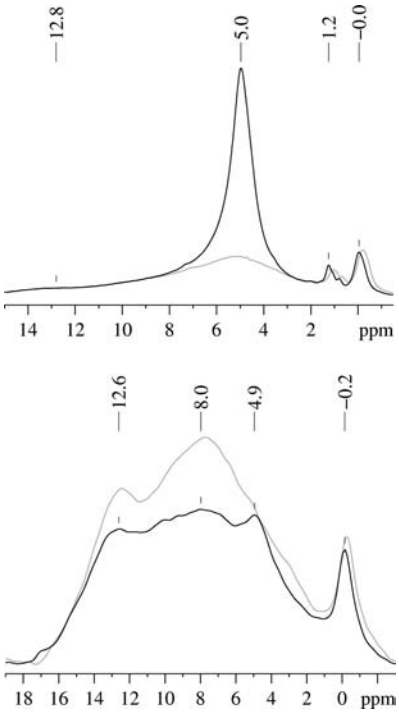

Figure 5. (Top) ^{1}H BD spectra recorded at 298 and 258 K (black and gray lines, respectively). (Bottom) ^{1}H−^{31}P−^{1}H double-CP spectra recorded at 298 and 258 K (solid and gray lines, respectively).

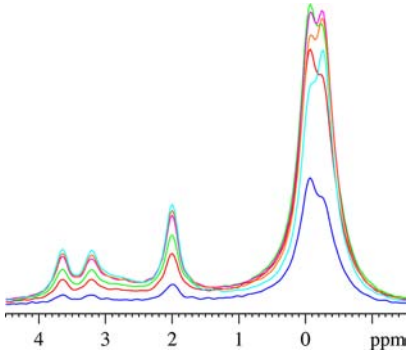

Figure 6. ^{31}P CP spectra recorded with contact times of 250 μs (blue), 750 μs (red), 1.25 ms (green), 2.25 ms (pink), 2.75 ms (orange), and 3.75 ms (cyan).

be 2. Given the ^{1}H mobility in the vicinity of these two sites, it is reasonable to compare the experimentally observed chemical shift of −0.3 ppm with the calculated average for P3 and P5 (−1.0 ppm), which is in excellent agreement. The apparently extreme value predicted for the chemical shift of P3 (−1.9 ppm) can be attributed to the strength of the hydrogen bond formed between P6 and P3 in the static structure (see Table 5).

As for the chemical shift anisotropies associated with P3, P5, and P6, the experimental powder patterns associated with isotropic chemical shifts of 0 and −0.3 ppm cannot be well approximated by a single powder pattern. Fitting each with a sum of two powder patterns identifies contributions from two markedly different environments (note that the same components were found independently in both cases). If we consider the average of the calculated chemical shift anisotropies associated with P3 and P5, then we find this to be in excellent agreement with one of the two environments determined experimentally. We tentatively assign the other environment to P6, and note that reduced chemical shift principal values (relative to the calculated anisotropy) are expected because of the molecular motion surrounding this site.

Experimental evidence can also be found in support of the reversal of the assignment of P1 and P4 (apatitic layer phosphorus sites, see Figure 1). These environments are quite similar, but the assignment can be verified by considering the ^{31}P{^{1}H} HETCOR experiment shown in Figure 7. [The

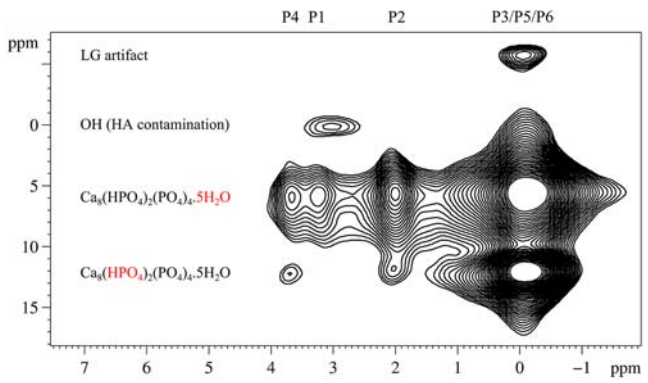

Figure 7. ^{31}P{^{1}H} HETCOR of OCP with FSLG in t_1. Note that a contact time of 300 μs was used to minimize the potential for spin diffusion and hence reveal only short-range correlations.

authors are aware that the correlation identified as due to hydroxyapatite (HA) contamination has also been attributed to proton migration from water molecules within the hydrated layer to orthophosphate units within the apatitic layer.[11] Our simplified assignment is based on the fact that the sample under study is a hydrolysis product which is known to contain hydroxyapatite impurities, and that the precise nature of this correlation has no direct relevance to the discussion.]

The presence of a correlation between the apatitic phosphorus site at 3.6 ppm and the ^{1}H signal at 12 ppm indicates that this phosphorus site is close to at least one of the HPO_4 sites. This is confirmed by the superior CP efficiency of the site at 3.6 ppm relative to the site at 3.2 ppm observed at low temperatures (see Supporting Information). Examination of the structure reveals that neither P1 nor P4 is within 7 Å of the hydrogen associated with P5, but P4 is considerably closer than P1 to the hydrogen associated with P6. In fact, P4 can see three times as many of these hydrogen sites as P1, as shown in Table 7, and we can therefore unequivocally assign the environment at 3.6 ppm to P4, and that at 3.2 ppm to P1, in full accord with the calculated assignment.

Finally, in Figure 8 we compare the predicted PXRD pattern of the revised 0 K structure of OCP with the room temperature experimental pattern, along with those predicted for the previously published crystal structure and for an optimized structure in which the lattice parameters were constrained to the values determined experimentally at room temperature in

Table 7. Proximities of P1, P4 to the Hydroxyl H of P6 Sites (within 7 Å)

site	$d_{P6-OH\cdots P}$ (Å)
P4	5.092
P1	5.708
P4	6.203
P4	6.621

dx.doi.org/10.1021/ja3017544 | J. Am. Chem. Soc. 2012, 134, 12508−12515

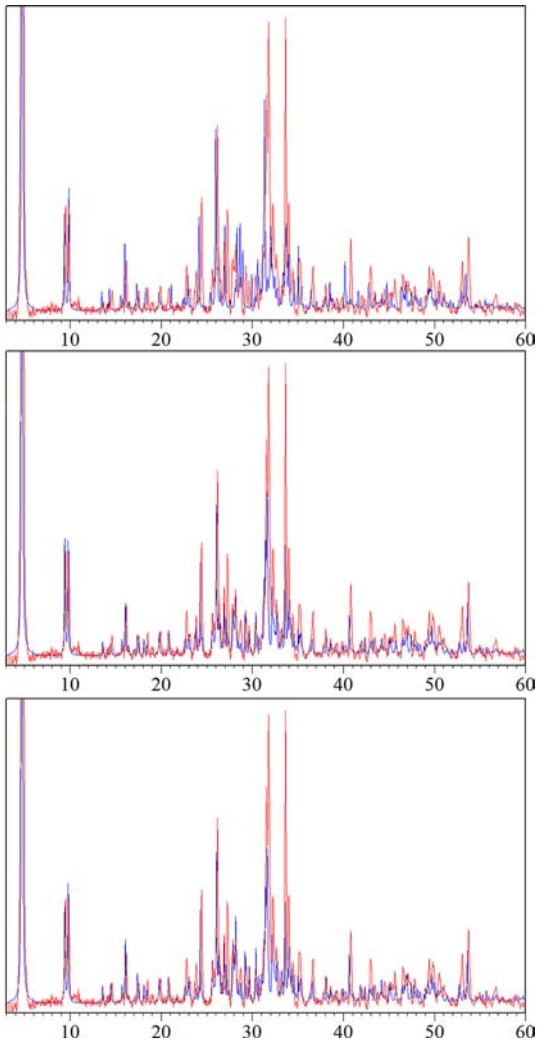

Figure 8. Experimental PXRD pattern of OCP (red) overlaid with the predicted PXRD patterns (blue) of the optimized (top), unoptimized (middle), and fixed-geometry optimized (bottom) OCP structures.

the original XRD study. The unconstrained 0 K structure is in reasonable agreement with the experimental pattern, despite the experimental pattern being recorded at room temperature. There are some reflections that do not fit as well as the original structure, which indicates that the 0 K structure has a slightly different geometry to the room temperature OCP structure. Unfortunately, it is not possible to record detailed low-temperature XRD data for this material, as this necessitates placing the sample under vacuum, which in turn causes the sample to dehydrate and the structure to collapse. It is therefore difficult to gain any information on how the unit cell geometry changes with temperature. [The PXRD pattern of OCP recorded at −70 K for 2θ between 3 and 12° shows that both the (100) and (200) reflections shift to lower 2θ at low temperature, consistent with expansion of the *a*-axis (see Supporting Information). Note that the range and quality of PXRD patterns that can be obtained under these conditions is extremely limited due to the buildup of ice in the absence of vacuum.] Instead, we may compare the experimental PXRD pattern with that predicted for the optimized structure with unit cell geometry fixed to that derived from room-temperature single-crystal XRD data. As Figure 8 shows, the agreement between these two powder patterns is excellent, and at least as good as the pattern predicted for the previously published structure. This geometry-optimized structure is overlaid with that from the unconstrained optimization in the Supporting Information; they are nearly identical, except for small differences in the unit cell geometry (rms 0.102 Å).

CONCLUSION

A 0 K refinement of the crystal structure of OCP and an unequivocal reassignment of the room temperature ^{31}P solid-state NMR spectrum have been presented. It was possible in the course of this investigation to assemble clear experimental evidence supporting the predictions of the DFT calculation once they were available, but without such guidance ambiguities in the data made a definitive assignment extremely challenging. The geometry-optimized structure of OCP resulting from the DFT calculations has revealed, for the first time, an extended hydrogen-bonding network within the hydrated layer of OCP. The identification of this network may facilitate a better understanding of the properties of OCP and its possible role in the formation of bone mineral.

ASSOCIATED CONTENT

Supporting Information

Overlays of OCP crystal structures, fully labeled OCP unit cell, details of H-bonding interactions in OCP before and after geometry optimization, comparison of geometry-optimized OCP structures with and without the SEDC-G06 module, comparison of calculated NMR parameters for various OCP structures, deconvoluted ^{31}P BD spectrum of OCP, variable-temperature ^{31}P NMR data, variable-temperature PXRD data, ^{31}P CSA lineshape fitting, and CIF file for the geometry-optimized structure of OCP. This material is available free of charge via the Internet at http://pubs.acs.org.

AUTHOR INFORMATION

Corresponding Author

mjd13@cam.ac.uk

Notes

The authors declare no competing financial interest.

ACKNOWLEDGMENTS

We thank Jonathan Yates (Oxford, UK), Dejan-Krešimir Bučar (Cambridge), David Jefferson (Cambridge, UK), and Derek Middlemiss (Cambridge, UK) for helpful discussions. We also thank the reviewers for their considered feedback and suggestions.

REFERENCES

(1) Harris, R. *Solid State Sci.* **2004**, *6*, 1025−37.
(2) *NMR Crystallography*, 1st ed.; Harris, R. K., Wasylishen, R. E., Duer, M. J., Eds.; John Wiley & Sons, Ltd.: Chichester, 2009.
(3) Nieto, C. I.; García, M. A.; Farrán, M. A.; Claramunt, R. M.; Torralba, M. C.; Torres, M. R.; Alkorta, I.; Elguero, J. *J. Mol. Struct.* **2012**, *1008*, 88−94.
(4) Pourpoint, F.; Gervais, C.; Bonhomme-Coury, L.; Azaïs, T.; Coelho, C.; Mauri, F.; Alonso, B.; Babonneau, F.; Bonhomme, C. *Appl. Magn. Reson.* **2007**, *32*, 435−57.
(5) Ashbrook, S.; Berry, A.; Frost, D. *J. Am. Chem. Soc.* **2007**, *129*, 13213−24.
(6) Brown, W. E.; Eidelman, N.; Tomazic, B. *Adv. Dent. Res.* **1987**, *1*, 306−13.
(7) Tseng, Y.-H.; Mou, C.-Y.; Chan, J. C. C. *J. Am. Chem. Soc.* **2006**, *128*, 6909−18.

(8) Bigi, A.; Cojazzi, G.; Gazzano, M.; Ripamonti, A.; Roveri, N. *J. Inorg. Biochem.* **1990**, *40*, 293−99.
(9) Brown, W. E.; Lehr, J.; Smith, J.; Frazier, A. *J. Am. Chem. Soc.* **1957**, *79*, 5318−19.
(10) Mathew, M.; Brown, W. E.; Schroeder, L. W.; Dickens, B. *J. Crystallogr. Spectrosc. Res.* **1988**, *18*, 235−50.
(11) Tseng, Y.-H.; Zhan, J.; Lin, K. S. K.; Mou, C.-Y.; Chan, J. C. C. *Solid State Nucl. Magn. Reson.* **2004**, *26*, 99−104.
(12) Harding, I. S.; Rashid, N.; Hing, K. A. *Biomaterials* **2005**, *26*, 6818−26.
(13) Brown, W. E. *Nature* **1962**, *196*, 1048−50.
(14) Chappell, H.; Duer, M.; Groom, N.; Pickard, C.; Bristowe, P. *Phys. Chem. Chem. Phys.* **2008**, *10*, 600−606.
(15) Elliott, J. C. *Structure and Chemistry of the Apatites and Other Calcium Orthophosphates*, 2nd ed.; Elsevier Science: Amsterdam, 1994; pp 24−25.
(16) Elliott, J. C. *Structure and Chemistry of the Apatites and Other Calcium Orthophosphates*, 2nd ed.; Elsevier Science: Amsterdam, 1994; pp 12−13.
(17) Hohwy, M.; Jakobsen, H. J.; Edén, M.; Levitt, M. H.; Nielsen, N. C. *J. Chem. Phys.* **1998**, *108*, 2686−94.
(18) Orr, R. M.; Duer, M. J. *J. Magn. Reson.* **2006**, *181*, 1−8.
(19) Clark, S. J.; Segall, M. D.; Pickard, C. J.; Hasnip, P. J.; Probert, M. I.; Refson, K.; Payne, M. C. *Z. Kristallogr.* **2005**, *220*, 567−70.
(20) Pickard, C.; Mauri, F. *Phys. Rev. B* **2001**, *63*, 1−13.
(21) Yates, J.; Pickard, C.; Mauri, F. *Phys. Rev. B* **2007**, *76*, 1−11.
(22) McNellis, E. R.; Meyer, J.; Reuter, K. *Phys. Rev. B* **2009**, *80*, 1−10.
(23) Grimme, S. *J. Comput. Chem.* **2006**, *27*, 1787−99.
(24) Perdew, J. P.; Burke, K.; Ernzerhof, M. *Phys. Rev. Lett.* **1996**, *77*, 3865−68.
(25) Profeta, M.; Benoit, M.; Mauri, F.; Pickard, C. J. *J. Am. Chem. Soc.* **2004**, *126*, 12628−35.
(26) Jeffrey, G. A. *An Introduction to Hydrogen Bonding*; Oxford University Press, Inc.: New York, 1997; pp 11−16.
(27) Santra, B.; Michaelides, A.; Fuchs, M.; Tkatchenko, A.; Filippi, C.; Scheffler, M. *J. Chem. Phys.* **2008**, *129*, 1−14.
(28) Kokalj, A. *Comput. Mater. Sci.* **2003**, *28*, 155−68.
(29) Webber, A. L.; Elena, B.; Griffin, J. M.; Yates, J. R.; Pham, T. N.; Mauri, F.; Pickard, C. J.; Gil, A. M.; Stein, R.; Lesage, A.; Emsley, L.; Brown, S. P. *Phys. Chem. Chem. Phys.* **2010**, *12*, 6970−83.
(30) Castro, M.; Seymour, V.; Carnevale, D.; Griffin, J. M.; Ashbrook, S. E.; Wright, P. A.; Apperley, D. C.; Parker, J. E.; Thompson, S. P.; Fecant, A.; Bats, N. *J. Phys. Chem. C* **2010**, 12698−710.
(31) Ashbrook, S. E.; Cutajar, M.; Griffin, J. M.; Lethbridge, Z. A. D.; Walton, R. I.; Wimperis, S. *J. Phys. Chem. C* **2009**, *113*, 10780−89.
(32) Cadars, S.; Lesage, A.; Pickard, C. J.; Sautet, P.; Emsley, L. *J. Phys. Chem. A* **2009**, *113*, 902−11.